PHYSICAL REVIEW C VOLUME 52, NUMBER 6 DECEMBER 1995

Radiative capture of polarized neutrons by polarized protons at $T_n = 183$ MeV

G. Xu,* S. F. Pate,† C. Bloch,‡ S. E. Vigdor, S. M. Bowyer,§ T. W. Bowyer,§ W. W. Jacobs, H. O. Meyer, E. Pierce, J. Sowinski, C. Whiddon,‖ and S. W. Wissink
Department of Physics, Indiana University, and Indiana University Cyclotron Facility, Bloomington, Indiana 47405

P. L. Jolivette
Department of Physics, Hope College, Holland, Michigan 49423

M. A. Pickar
Department of Physics, University of Kentucky, Lexington, Kentucky 40506

(Received 13 March 1995)

In order to provide a quantitative test of theoretical calculations incorporating meson-exchange currents and intermediate Δ resonances, we measure the normal-component spin correlation coefficient C_{NN}, the differential cross section $d\sigma/d\Omega$, and the neutron and proton analyzing powers A_n and A_p, each as a function of angle, for $\vec{n}\vec{p}\to d\gamma$ at $T_n=183$ MeV. Our $\vec{n}\vec{p}\to d\gamma$ results, combined with the previous cross section and photon asymmetry data collected in the past decade, place quite strong constraints on model calculations. Our data are in excellent agreement with theoretical predictions by Jaus and Woolcock that incorporate meson-exchange and isobar current effects and relativistic corrections, signifying great recent progress in our understanding of these effects in the nucleon-nucleon system.

PACS number(s): 25.40.Lw, 24.70.+s, 13.75.Cs, 21.30.+y

I. INTRODUCTION

Radiative capture of neutrons by protons, or its time-reversed reaction, deuteron photodisintegration, is one of the simplest, yet most fundamental nuclear processes. The primary interaction is electromagnetic, and is thus well understood; the leading effects of the strong interaction, occurring between two nucleons, are also well characterized. Thus, observables for this reaction, if measured with sufficient precision, can provide a sensitive probe to "corrections" associated, for example, with the role of subnucleonic degrees of freedom and with relativistic effects.

If the momentum transfer (q) in the reaction is not too high, one would hope that the role of subnucleonic degrees of freedom could be efficiently described in terms of the contributions of meson-exchange currents (MEC's) and isobar currents (IC's) to the reaction amplitude. The effects of meson exchange between nucleons in diagrams in which the photon couples directly to the nucleons are already implicitly included via Siegert's theorem[1] in any calculation employing a realistic nucleon-nucleon (NN) potential. However, the explicit coupling of the photon to exchanged mesons and intermediate-state Δ's is not so included. The electric dipole coupling of the photon to the nucleons is known to dominate the reaction at low momentum transfer; however, for $q \gtrsim 1$ fm^{-1} the explicit MEC and IC contributions begin to introduce appreciable magnetic (mainly $M1$) transition amplitudes [2]. The different sensitivities of the magnetic and electric transitions to the spin state of the nucleons suggest that a full investigation of the role of MEC and IC contributions requires polarization as well as cross section measurements at sufficiently high q.

In recent years, there have been several polarization observable measurements for deuteron photodisintegration and np radiative capture at intermediate energies [3–5]. While the results generally agree well with theoretical calculations that incorporate MEC's and IC's [2,6–8], the quantities measured were not always very sensitive to the role of subnucleonic degrees of freedom (for example, see [3]).

The goal of the present work was to measure a polarization observable with particularly strong sensitivity to MEC and IC contributions to deuteron photodisintegration, in order to test quantitatively the validity of calculations of these effects. The effects are manifested primarily via magnetic ($M1$) transition amplitudes, which couple spin *singlet np* states to the bound ^3S and ^3D states of the deuteron. In contrast, the dominant electric dipole transition couples spin *triplet np* states to the deuteron. The magnetic transitions are thus most directly distinguished by observables which are sensitive to the relative orientations of the n and p spins, i.e., to the so-called spin correlation coefficients C_{ij} in $\vec{n}\vec{p}\to d\gamma$. Measurements of np radiative capture have never previously been made utilizing both polarized beams and polarized targets. In the present experiment we have utilized neutron beam and proton target polarizations normal (N) to the $\vec{n}\vec{p}\to d\gamma$ reaction plane, and have thus measured the normal-component spin correlation coefficient, defined as the relative difference in cross sections for n and p spins parallel vs antiparallel:

---

*Current address: Wright Nuclear Structure Laboratory, Yale University, 272 Whitney Ave., New Haven, Connecticut 06511.

†Current address: Laboratory for Nuclear Science, Massachusetts Institute of Technology, Cambridge, Massachusetts 02139.

‡Current address: Indiana University Proton Therapy Center, Department of Radiation Oncology, Indiana University School of Medicine, IN 47408.

§Current address: Battelle-Pacific Northwest Laboratory, P.O. Box 999, P8-08, Richland, WA 99352.

‖Current address: Department of Radiation and Cellular Oncology, University of Chicago Medical Center, Chicago, IL 60637.

0556-2813/95/52(6)/2859(16)/$06.00

$$C_{NN}(\theta)\equiv\frac{d\sigma/d\Omega_{\uparrow\uparrow}(\theta)+d\sigma/d\Omega_{\downarrow\downarrow}(\theta)-d\sigma/d\Omega_{\uparrow\downarrow}(\theta)-d\sigma/d\Omega_{\downarrow\uparrow}(\theta)}{d\sigma/d\Omega_{\uparrow\uparrow}(\theta)+d\sigma/d\Omega_{\downarrow\downarrow}(\theta)+d\sigma/d\Omega_{\uparrow\downarrow}(\theta)+d\sigma/d\Omega_{\downarrow\uparrow}(\theta)}=\frac{1}{P_nP_p}\frac{N_{\uparrow\uparrow}+N_{\downarrow\downarrow}-N_{\uparrow\downarrow}-N_{\downarrow\uparrow}}{N_{\uparrow\uparrow}+N_{\downarrow\downarrow}+N_{\uparrow\downarrow}+N_{\downarrow\uparrow}},$$

where $d\sigma/d\Omega_{\uparrow\downarrow}$ and $N_{\uparrow\downarrow}$ are the $np\rightarrow d\gamma$ differential cross section and normalized yield, respectively, for neutron spin up, proton spin down, at a given γ angle. The other terms are similarly defined. P_n and P_p are beam and target polarizations, respectively.

The sensitivity of C_{NN} to magnetic transitions can be understood qualitatively. For the $S=1$ (triplet) np states coupled to the deuteron by electric transitions, the n and p spins are predominantly parallel, and hence $C_{NN}\geqslant 0$. For example, consider the angular momentum coupling constraints for the ^3P states that couple to the $^3S_1$ deuteron ground state. Noting that the orbital angular momentum projection normal to the plane is restricted to ± 1 for the $L=1$ parts of the incident plane wave, $^3P_2$ gives $C_{NN}=2/5$, $^3P_1$ gives $C_{NN}=0$, and $^3P_0$ gives $C_{NN}=1$. In contrast, all *singlet np* states, such as $^1S_0$ and $^1D_2$, which are coupled to the deuteron by $M1$ transitions, give a value of $C_{NN}=-1$. Therefore, we may expect this observable to become more negative with increasing bombarding energy as MEC and IC terms begin to contribute significantly. Even small additional currents can have a significant effect on the spin correlation coefficients. The substantial sensitivity of C_{NN} to MEC and IC effects has been confirmed theoretically in recent calculations by Jaus and Woolcock [6] and Schmitt and Arenhövel [2]. The calculations will be discussed later in this paper.

We chose to measure C_{NN} for np radiative capture at a bombarding energy $T_n=183$ MeV (corresponding to $E_\gamma=95$ MeV for deuteron photodisintegration) for several reasons. This energy is high enough that MEC and IC effects are expected to be significant, yet low enough that the inclusion of only a small number of relatively light mesons and only the $\Delta(1232)$ baryon resonance should be a good approximation in the theoretical calculations. Another consideration that influenced the choice of bombarding energy was the desire to minimize background that might arise from π^0 production on protons bound inside contaminant nuclei in the polarized proton target. It is also useful to note that the measurement of C_{NN} requires that the neutron beam and proton target be simultaneously polarized. By reversing the beam and target spins independently, we were able to extract, at the same time as C_{NN}, the neutron and proton analyzing powers A_n and A_p (each defined as the relative difference in cross sections for the corresponding nucleon spin up vs down):

$$A_n(\theta)=\frac{1}{P_n}\frac{N_{\uparrow\uparrow}-N_{\downarrow\downarrow}+N_{\uparrow\downarrow}-N_{\downarrow\uparrow}}{N_{\uparrow\uparrow}+N_{\downarrow\downarrow}+N_{\uparrow\downarrow}+N_{\downarrow\uparrow}},$$

$$A_p(\theta)=\frac{1}{P_p}\frac{N_{\uparrow\uparrow}-N_{\downarrow\downarrow}-N_{\uparrow\downarrow}+N_{\downarrow\uparrow}}{N_{\uparrow\uparrow}+N_{\downarrow\downarrow}+N_{\uparrow\downarrow}+N_{\downarrow\uparrow}}.$$

Although the analyzing powers are not predicted to be particularly sensitive to MEC and IC effects, they help to constrain ambiguities that may arise in other aspects of the calculations. We designed the experiment to measure C_{NN} at a number of angles to an accuracy of ±0.05, i.e., with sufficient precision to distinguish among various levels of inclusion of MEC, IC and relativistic effects in the theoretical calculations.

The spin observable results of this experiment have been published previously [9]. The present paper presents a more detailed description of the experimental techniques and the assessment of systematic errors for the spin observable results. In particular, these results have been renormalized, in comparison with Ref. [9], in light of an improved calibration [10] of the neutron beam polarization. In addition, we report here the absolute differential cross sections for $np\rightarrow d\gamma$, as determined in our experiment.

II. EXPERIMENTAL APPARATUS AND DATA ACQUISITION

A. Experimental overview

The experiment was carried out in the polarized neutron facility (PNF) at the Indiana University Cyclotron Facility. The data acquisition was completed through three production runs, for a total of roughly 1000 h of beam time.

A schematic illustration of the experimental setup used for production running is shown in Fig. 1. The experiment used a polarized neutron beam and a polarized proton target (PPT). A "dummy" target, which simulated the nonhydrogenic components of the in-beam materials of the PPT, was used to measure background, including quasifree $A(n,d\gamma)$ reactions initiated on protons bound in contaminant nuclei in the PPT. In order to suppress background, the outgoing deuterons and photons were measured in coincidence. The deuterons were detected near 0° by ΔE and E plastic scintillators and by four multiwire proportional chambers (MWPC's; labeled $X1$, $Y1$, $X2$, and $Y2$ in Fig. 1). A veto scintillator V, placed behind the E detector, was used to identify and veto high-energy protons produced by the neutron beam. The coincident γ's were detected by an array of 160 Pb-glass Čerenkov counters, spanning laboratory angles from 34° to 109° to the left of the beam and from 79° to 124° to the right. (The left-right asymmetric arrangement of Čerenkov counters was chosen to cover the entire angle range of interest, while avoiding photon attenuation through thick metal posts that constituted part of the superconducting magnet assembly inside the PPT Dewar.) The relative neutron flux was monitored for each beam-target spin state independently by two pairs of in-beam scintillators, only one of which—S_0 and S_1—is shown in Fig. 1. The beam and target polarizations were monitored continuously by detecting np elastic scattering coincidences from the PPT, with proton detectors on the beam left and neutron detectors on the right. The performance of all the detectors is described in more detail in ensuing sections.

B. Beam and targets

Details of the PNF, the PPT, and the dummy target have already been discussed in Refs. [11,12]. Here we briefly

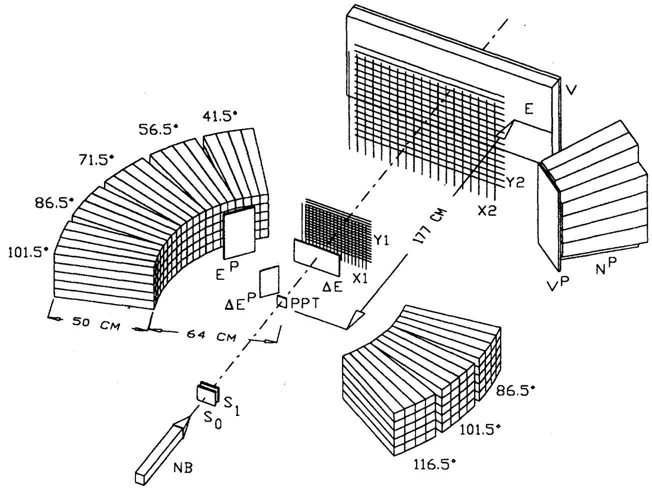

FIG. 1. Scale rendering of the detector setup. Each stack of Pb-glass detectors is labeled by its central laboratory polar angle. The polarized target is indicated schematically and labeled by PPT. Details are discussed in the text.

summarize their properties relevant to the present experiment. The neutron beam was produced via the $^2\mathrm{H}(\vec{p},\vec{n})2p$ reaction at $\theta_{\mathrm{lab}}=10°$, initiated by 200 MeV polarized protons on a 20 cm thick liquid deuterium target. Neutrons selected for study (by their time of flight) had a mean kinetic energy of 183 MeV, with an energy spread of $\simeq$15 MeV full width at half maximum (FWHM). The vertical polarization of the neutron beam was typically 0.50–0.65, and its direction was reversed every 15 s. The primary proton beam was pulsed, with a time separation of 57 ns between consecutive pulses. The average primary beam current was 224 nA, giving about 4×10^6 neutrons/s in a beam spot 5 cm wide by 7 cm high at the target position.

The PPT, of "spin-refrigerator" type [13], contained 1.0 g/cm^2 of the target material yttrium ethyl sulfate [$\mathrm{Y(C_2H_5SO_4)_3\cdot 9H_2O}$, or YES], doped with Yb. It was repolarized twice per day by rotating the target crystals at about 40 Hz in the presence of a 1.2 T polarizing field at a temperature ~0.5 K [12]. During data acquisition, the target was held stationary in a reduced magnetic field (0.059 T). The target could be set in either one of two modes: normal (NRM) mode, in which the holding field direction is kept parallel to that of the proton polarization, or adiabatic fast passage (AFP) mode, in which case they are antiparallel [11]. The relaxation time of the polarization at the holding field strength used was typically 80–150 h, and the time-averaged polarization during running periods was about 0.40.

In comparison with its use in Ref. [11], the PPT was placed further downstream of the neutron production target (4.7 m instead of 4.3 m), and the PPT Dewar was rotated by ~45° so that the copper and stainless steel posts of the PPT magnet assembly would not block photons emitted toward the Pb-glass detectors. The neutron beam collimator was modified, in accordance with the change in target position, in order to keep the neutron beam size at the target position the same as that of the YES crystals.

In addition to the PPT and the dummy target, a few auxiliary targets were also used in this experiment for calibration and setup purposes. These included a 0.452 g/cm^2 $\mathrm{CH_2}$ target, of transverse area much larger than that of the beam spot. Because this target contained relatively more hydrogen and fewer contaminant nuclei than the PPT, it was used to calibrate the gain of the np polarimeter neutron detectors (see Sec. II C), and the absolute neutron flux, by detecting the forward-going high-energy protons from np elastic scattering events induced in the target (see Sec. III D). To measure background caused by the contaminant carbon nuclei in the $\mathrm{CH_2}$ target and by other materials along the beam path (e.g., the ΔE scintillator), data were taken with a 0.432 g/cm^2 carbon target and also without any target.

C. Detectors

1. Photon detectors

The 160 Pb-glass Čerenkov counters used in the experiment were blocks of Schott F2 glass, measuring 4.2×6.4 cm^2 on the front face, 6.4×6.4 cm^2 on the back face, and 50 cm in length. This length corresponds to about 10 r.l. for the photon energies of interest. Each block was attached to an EMI 9839B photomultiplier tube that contained 12 dynodes. A test using the tagged photon facility at the University of Illinois [14] showed that the energy resolution of an individual detector for photons (energy 70 MeV) incident near the center of its front face was typically 34%. The test also determined the equivalent photon energy for the cosmic ray peak seen by each detector, which allowed us in the subsequent experiment to calibrate photon energies by detecting cosmic rays interspersed with the reaction product photons. The output of each Pb-glass counter was fed through an individual constant-fraction discriminator (CFD), with a threshold set at $E_\gamma\sim18$ MeV. As can be seen in Fig. 1, these detectors were arranged into eight stacks, each of which was four blocks wide by five blocks high. The front face of each stack subtended a geometric solid angle of 0.127 sr. For a $d\gamma$ event, the Pb-glass detector with the largest recorded pulse height was chosen to determine the photon's angular information, but the pulse height in the neighboring cells (in the same stack) was added to the largest pulse height to determine the photon energy. The overall efficiency for each stack to detect $d\gamma$ photons was typically 89% (see Sec. III D 3).

The analog signals and CFD timing signals from the 160 Pb-glass detectors were multiplexed into 32 channels, each of which contained inputs from 5 nonneighboring Pb-glass counters. The counters that actually fired for a given event were determined from the pattern of latches set by the CFD outputs for each counter. The analog signals were fed to analog-to-digital converters (ADC's) with ac-coupled inputs to filter out low-frequency noise.

The relative gains and timing of all the Pb-glass counters were monitored continuously throughout the experiment by acquiring cosmic ray events interspersed with $np\rightarrow d\gamma$ events. Since only small gain shifts were observed, the gain matching (by high voltage adjustment) was performed once at the beginning of each production running period and then once per day during the run. The time resolution of each Pb-glass detector, measured using cosmic rays, was better than 1.0 ns.

The Pb-glass detectors were quite insensitive to most of the hadrons (p, d, n, $\pi^\pm$) produced in the beam-target interactions, as these particles were too slow to generate Čerenkov light and had a very small probability to generate secondary photons above 18 MeV in nuclear reactions. Thus, despite the presence of a high neutron flux, each individual Pb-glass detector fired at a singles rate of only ~200 Hz.

2. In-beam deuteron detectors

The ΔE and E scintillators were 0.32 and 7.0 cm thick, respectively. The dimensions of the ΔE and E scintillators, centered about 0°, were chosen so that all deuterons from the $np \rightarrow d\gamma$ reaction (falling within a cone of laboratory half-angle 9°) could be detected by both detectors and would all be stopped in the E scintillator. The veto (V) scintillator had the same transverse dimensions as the E detector, but was only 0.64 cm thick. The E and V scintillators were each viewed by four photomultipliers (two on the left and two on the right end of the E scintillator and four on the top of the V scintillator), whose gains were matched during the experiment by recording the pulse heights produced, as a function of impact position, by forward-angle high-energy protons originating from np elastic scattering in the target. The summed pulse height from the four phototubes was found in each case to be quite uniform (variation $\lesssim 10\%$) over the entire active area of the scintillator.

Four in-beam multiwire proportional chambers were used for angle measurements and ray-tracing forward-going charged particle tracks back to the target location. The wire spacings of the $X1$, $Y1$, $X2$, and $Y2$ chambers were 1.95, 2.54, 4.36, and 5.45 mm, respectively. The active areas accepted all deuterons of interest. When the wire chambers were plateaued for the deuterons of interest, they were able to withstand the full neutron beam intensity with acceptable ($<5\ \mu$A) leakage currents. The deuteron detection efficiency for each individual wire chamber was nearly 100%. The overall probability for a $d\gamma$ deuteron to yield at least one hit in each of the four wire chambers was 97.8%, averaged over all of the PPT runs. The overall efficiency for detecting forward-going protons from np elastic scattering events was somewhat lower (93.6%).

3. Flux monitor detectors

There were two monitors used for measuring the relative neutron flux for each beam-target spin combination. Each flux monitor consisted of a pair of in-beam plastic scintillator paddles of transverse dimensions larger than the beam: a thinner one placed upstream to veto charged particles and a thicker one downstream to detect neutrons (via nuclear reactions within the paddle). Flux monitor 1 was placed immediately downstream of the exit of the neutron collimator, while flux monitor 2 was placed behind the V detector. Relative measurements between the two monitors agreed typically to within ±0.1%.

4. np polarimeter detectors

The np polarimeter was used to monitor the neutron beam and proton target polarizations, by measuring np elastic scattering induced in the PPT. The polarimeter consisted of an array of 16 liquid scintillator neutron detectors N^P, to the right of the beam, and a ΔE^P-E^P plastic scintillator telescope to detect the coincident protons on the left (see Fig. 1). A thin plastic veto scintillator V^P was placed in front of the neutron detectors to veto charged ejectiles.

Each of the 16 neutron detectors [11] was 8 cm wide by 10 cm high at its front face, 40 cm deep, and 10 cm wide by 12.5 cm high at the rear. The 16 detectors formed three columns (6 detectors each in columns 0 and 1, and 4 in column 2) centered, at midplane, about laboratory polar angles of 33.3°, 36.4°, and 39.5°, respectively. The planar front face of the detector array was placed 1.46 m from the target. The neutron detectors were gain matched by detecting pp coincidences induced by a secondary proton beam (obtained by turning off a sweeping magnet in the PNF) on the CH_2 target placed at the usual PPT position. In this matching procedure, the phototube high voltages were adjusted to yield proton pulse heights that varied with the angle of the liquid scintillator cell in the manner expected from pp elastic scattering kinematics.

The ΔE^P and E^P detectors were centered at a laboratory angle of 51.0°. The transverse dimensions of both these scintillators were large enough to detect almost all ($\gtrsim 98.5\%$) free-scattering protons in coincidence with the neutrons detected in N^P, even after allowing for multiple scattering of the protons and their deflection in the magnetic holding field of the PPT.

D. Event types

The detectors described above allowed us to record the following types of events simultaneously.

(1) $np \rightarrow d\gamma$ candidate events: events in which ΔE, E, at least three of the four wire chambers, and at least one Pb-glass Čerenkov counter fired in coincidence, while the veto detector (V) and the upstream scintillator S_0 did not fire.

S_0 was used to reject events initiated by charged particles. By requiring only three wire chambers to fire, we were able to keep track of the efficiency of each chamber on line. During the final production period, we removed the wire chamber requirement entirely from the hardware trigger for both $d\gamma$ and "proton" (see below) events, for diagnostic purposes. However, we still recorded wire chamber hit patterns for each event.

(2) "Proton" events: prescaled (by a factor of 400) events in which ΔE, E, at least three of the four wire chambers, and V fired in coincidence, while S_0 did not fire.

The "proton" events were used not only to monitor the gains of the in-beam scintillator phototubes, but also to calibrate the absolute neutron flux using the known np elastic backscattering cross sections (see Sec. III D).

(3) Cosmic ray events: events in which at least one Čerenkov counter and at least one of five plastic scintillator trigger paddles placed on top of the Pb-glass stacks fired in coincidence, while E did not fire.

For each cosmic ray event, we recorded the pulse height and timing information for all of the Pb-glass detectors, in order to monitor their gains and timing continuously throughout the experiment. In addition, for these events we also recorded the pulse heights for all in-beam and np polarimeter scintillators (even though these detectors had not fired in principle), in order to keep track of their 60 Hz noise patterns. The phase of each event arrival within a 60 Hz cycle was monitored for all event streams via the amplitude of a "sawtooth" wave generated in synchronization with the ac power. The event loci in the spectra of sawtooth wave vs noise amplitude for the in-beam and polarimeter scintillators provided high statistics templates that allowed us to subtract the noise or pedestal contribution event by event from the ADC outputs recorded for those detectors for other types of events.

(4) Flux monitor events: prescaled (by a factor of 1000) events in which the rear paddle of the flux monitor scintillator pair fired, while the front paddle did not. The time between the rear paddle signal and the cyclotron rf signal was recorded for each event, in order to monitor the neutron beam energy spectrum.

(5) np polarimeter events: events in which the proton telescope elements ΔE^P and E^P fired in coincidence with at least one of the 16 neutron detector cells N^P, while S_0 and V^P did not fire.

E. Data acquisition

The analog, logic, and timing signals from the detectors described above were digitized by CAMAC modules and then read into a microVAX III computer via an MBD-11 branch controller. The data were also recorded on magnetic tape for subsequent off-line analysis. The software package XSYS [15] was used for both data acquisition and off-line analysis.

The $\vec{n}\vec{p}\rightarrow d\gamma$ data acquisition was divided into "cycles." A typical cycle lasted roughly 24 h and included the following: 2–3 h of PPT repolarization, followed by roughly 7 h of data acquisition with the PPT in either NRM or AFP mode; another 2–3 h of target repolarization, followed by roughly 7 h of data acquisition with the PPT mode switched (from NRM to AFP or vice versa); finally, 4–5 h of data acquired with the dummy target. In all, 26 such cycles of data were taken. These included 12 cycles from the first production run, during which the PPT was always kept in NRM mode, due to a hardware problem with the nuclear magnetic resonance coil needed to effect the AFP transition.

During each cycle, the PPT holding field was adiabatically reversed every 15 min (a process that took ~40 s) to flip the spin orientation of the polarized protons. Special care was taken to correct for any detector gain shifts caused by this field reversal. Inside the target wall (radius 15 cm), the holding field was approximately 0.059 T. Outside the target wall, the field decreased rapidly with distance, to a typical level of a few $\times 10^{-4}$ T to 10^{-5} T near the photomultiplier tubes of the various scintillators. Although all photomultiplier tubes used in this experiment were magnetically shielded, the change in residual magnetic field caused by the target field reversal nonetheless produced appreciable gain shifts in the tubes attached to the Pb-glass detectors and to the neutron detectors used for the polarimeter. The cosmic ray events allowed us to track continuously and to correct for the gain shifts of the Pb-glass detectors, which ranged from 5% to 20%. The gain changes in the neutron detectors were measured in a separate run, utilizing the secondary proton beam. For these measurements, we observed pp elastic scattering coincidences induced on the flux monitor veto scintillator S_0 (see Fig. 1), with the forward-going protons traveling to the neutron detectors along paths that did not traverse the PPT Dewar, and thus undergoing negligible deflection from the holding field. By reversing the PPT field in the usual way, we observed neutron detector gain shifts of 1–2 %, which were later corrected using software gains and thresholds.

The magnetic holding field also deflected the paths of charged particles as they exited the PPT; for the $\vec{n}\vec{p}\rightarrow d\gamma$ deuterons of interest, this effect is small (<0.5°) and easily calculable. In addition to correcting for the effects of the target field on an event-by-event basis in the data replay, we used the comparison of the results obtained in NRM (target polarization parallel to the holding field) and AFP (antiparallel) modes to study and cancel any residual field-dependent systematic errors (see Sec. V).

In order to get further information about the sizes of potential systematic errors associated with reversal of the PPT holding field, we took three additional cycles of data with the YES target *unpolarized*, but the holding field on and flipping as usual. In the absence of systematic errors, the target analyzing power asymmetry and the product of target polarization and spin correlation measured in these extra cycles should be exactly zero (see Sec. V A).

III. DATA ANALYSIS

The primary goal of the data analysis was to identify the $\vec{n}\vec{p}\rightarrow d\gamma$ events induced on the hydrogen component in the PPT, to subtract any background contributing to this event sample, and to deduce the cross section $d\sigma/d\Omega$ and the normal-component spin observables A_n, A_p, and C_{NN}. The main procedures are discussed below.

A. Software corrections to the raw data

Certain corrections had to be applied to the raw data before we could proceed to identify events of interest. These included ac noise and pedestal subtraction from ADC values, software corrections for gain differences among the detectors, time-offset alignment for the time-to-digital converter (TDC) values from the detectors, and corrections for effects of the PPT holding field.

The ac noise and pedestal subtractions for ADC's from the in-beam and np polarimeter scintillators have been described in Sec. II C. In practice, the ac noise pattern and the ADC pedestal values were updated for every 20 000 cosmic ray events (corresponding to ~30 min intervals). Noise subtraction was not necessary for the Pb-glass counters, for which the ADC inputs were ac coupled.

The detector gains were monitored and were roughly matched online by the techniques described in Sec. II. Software corrections were used to compensate for small remaining gain differences among different phototubes and to take account of the measured gain changes with time and with PPT holding field polarity. Field-dependent gain shifts were appreciable only for the Pb-glass and neutron detectors. The software gain factors were updated for each individual run for the in-beam scintillators, for each data cycle in the case of the Pb-glass counters, and for the three different production running periods in the case of the np polarimeter detectors. An additional software correction compensated for the small measured position dependence observed for the E-detector summed pulse height (see Sec. II C 2).

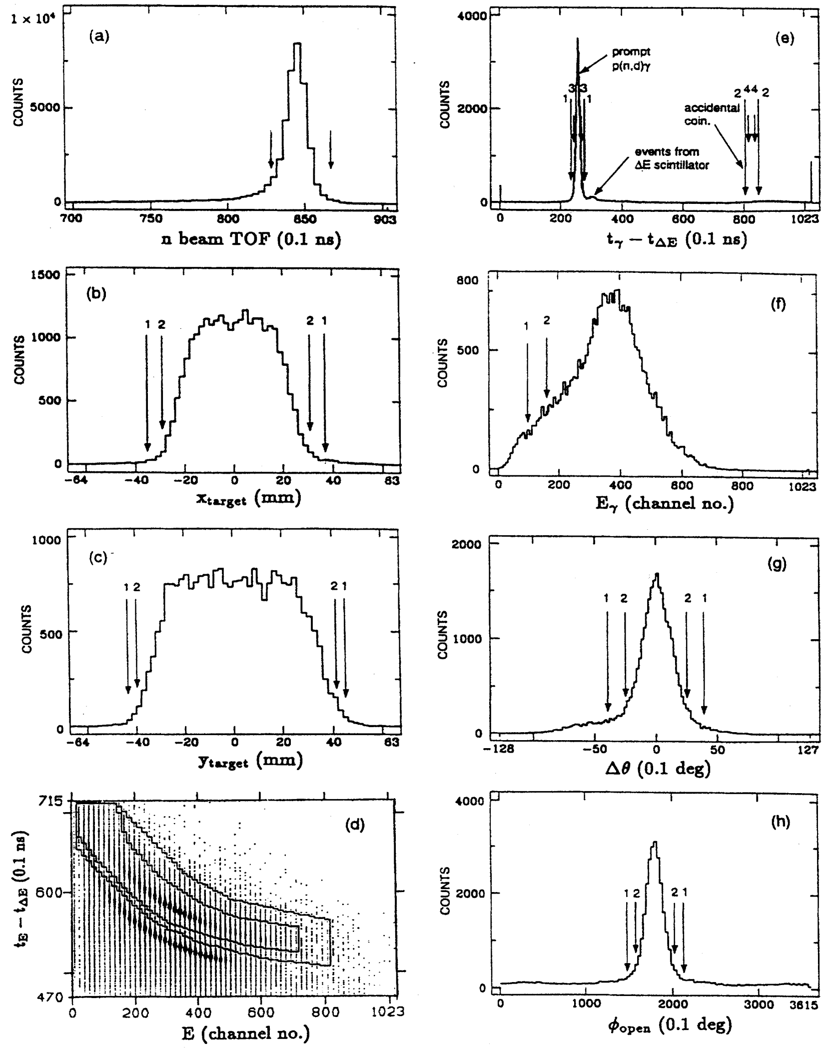

FIG. 2. $np \rightarrow d\gamma$ spectra (a)–(h) for events that gave only a single hit in each MWPC and their corresponding software cuts (loose, labeled 1, and tight) used for the selection of $np \rightarrow d\gamma$ events. Events from all 160 Pb-glass counters are included in all the spectra. In (a)–(c), (e)–(h), all loose cuts except the neutron energy cut and the cut corresponding to the displayed spectrum itself have been applied to select events. In (d), only event origin, time correlation, and photon energy cuts have been applied.

The effect of the PPT holding field on the deuteron motion was also calculated and corrected in software. Since the bend angle was always small ($<0.5°$), we were able to estimate it with sufficient accuracy using a simplified model that assumed a uniform 0.059 T field within a radius of 15 cm from the target center and zero field outside.

The timing offsets for the 160 Pb-glass detector TDC's were calibrated every two cycles using the online $\vec{n}\vec{p} \rightarrow d\gamma$ events themselves. After applying a series of software cuts to select these events (see Fig. 2), we observed a narrow peak in the t_γ-$t_{\Delta E}$ spectrum for each Pb-glass detector, corresponding to the $\vec{n}\vec{p} \rightarrow d\gamma$ events initiated in the PPT (see Fig. 3). We adjusted the software timing offsets so that the peaks in the t_γ-$t_{\Delta E}$ spectra were aligned for all 160 counters. This procedure corrected not only for phototube and cable length differences among the photon counters, but also for kinematic differences in the flight time of the coincident deuterons from the target to the ΔE scintillator.

The signal output time from the single ΔE phototube, relative to the arrival time of a charged particle at the ΔE scintillator, varied with the hit position of the particle. This dependence was measured by observing the time difference between the E and ΔE scintillators for the forward-going proton events from np elastic scattering in the PPT, as a function of hit position as deduced from the wire chamber information. The E-scintillator time was taken to be the average value of the arrival times from its four phototubes, resulting in a negligible spatial dependence of the arrival time for the central region of the detector. The small observed position dependence of the ΔE time signal (≤ 0.5 ns within the region of interest for forward-going deuterons) was subsequently corrected in software.

The time spectra for the neutron detectors (with respect to the E^P scintillator) were measured online for pp elastic scattering events in CH_2 target runs. We adjusted software timing offsets for each liquid scintillator cell so that all of the pp scattering timing peaks were aligned.

B. $\vec{n}\vec{p} \rightarrow d\gamma$ data analysis

1. Identification of $\vec{n}\vec{p} \rightarrow d\gamma$ events

We identified $\vec{n}\vec{p} \rightarrow d\gamma$ events via a series of software cuts and conditions, most of which are illustrated in Fig. 2. In order to estimate systematic errors associated with possible spin-dependent removal of events by software cuts, we used two sets of cuts (loose and tight) on all variables except the

ΔE signal arrival time with respect to the cyclotron rf, which determines the neutron bombarding energy range accepted. The physical interpretations of the loose cuts are as follows.

(a) Neutron beam energy: A cut was applied on the neutron beam time of flight [Fig. 2(a)] TOF$=t_{\mathrm{rf}}-t_{\Delta E}+\Delta t_d$, where t_{rf} and $t_{\Delta E}$ are the times for the rf signal and ΔE scintillator, respectively, and Δt_d is the *calculated* flight time of deuterons from the PPT to the ΔE scintillator, based on $np \to d\gamma$ kinematics as a function of lead glass stack number for the observed coincident photon. This cut selects incident neutrons approximately in the energy range 170–193 MeV (mean energy$=$183 MeV) [11].

(b) Event origin: Wire chamber hit information was used to ray-trace outgoing charged particle trajectories back to the target plane. Cuts were applied on the x and y distributions of transverse event origin coordinates to eliminate events that originated outside the target volume [Figs. 2(b)–2(c)].

(c) Particle identification: Forward-going deuterons were distinguished from protons by gates on the time of flight of particles (from ΔE to E scintillator) vs pulse height in the E scintillator [Fig. 2(d)] or on ΔE pulse height vs E pulse height.

(d) Timing correlation: A cut was placed on t_γ-$t_{\Delta E}$ to select only those $\vec{n}\vec{p} \to d\gamma$ events initiated on the PPT [those in gate 1 in Fig. 2(e)]. The time resolution was sufficient ($\sim$1 ns FWHM) to discriminate cleanly against $\vec{n}p \to d\gamma$ events initiated on hydrogen in the ΔE scintillator itself. The prompt gate was displaced by 57 ns (the separation between successive beam bursts), yielding gate 2 in Fig. 2(e) to select an event sample for accidental coincidence subtraction.

(e) Photon energy: The energy of photons from $\vec{n}\vec{p} \to d\gamma$ events ranged from 70 to 120 MeV over the angle range covered. A loose software threshold at $\sim$22 MeV was applied to eliminate accidental coincidences with the abundant low-energy background γ's [Fig. 2(f)].

(f) θ_d vs θ_γ: The observed photon angle was used to calculate the expected deuteron angle, using two-body kinematics. The difference $\Delta\theta$ between this value and the deuteron angle measured with the wire chambers was restricted by the loose cut to $\sim\pm 4^\circ$ [Fig. 2(g)] for the selected events.

(g) Coplanarity: The d and γ should be coplanar with the neutron beam if they arise from a two-body final state. In the analysis, the difference in measured azimuthal angles of the deuteron and the photon, ϕ_{open}, was restricted by a loose cut to $180^\circ \pm 33^\circ$ [Fig. 2(h)]. This cut, together with that on $\Delta\theta$, eliminated most of the background from quasifree $A(\vec{n},d\gamma)$ reactions induced on contaminant nuclei in the PPT.

(h) E_d vs θ_γ: A two-dimensional cut was applied to select events in which E_d was correlated with θ_γ as expected from two-body kinematics.

Two types of background were subtracted from the event sample selected by the above cuts. Accidental coincidences between a charged particle from one beam burst and a photon from the next (57 ns later) were recorded [those in gate 2 in Fig. 2(e)] and were then subtracted from the prompt coincidences that satisfied the same cuts on other variables. Any remaining background was then removed by subtracting the yields obtained for the dummy target, after application of identical software gates to those above, subtraction of dummy-target accidentals, and normalization to the same deadtime-corrected integrated neutron flux as was recorded for the PPT runs.

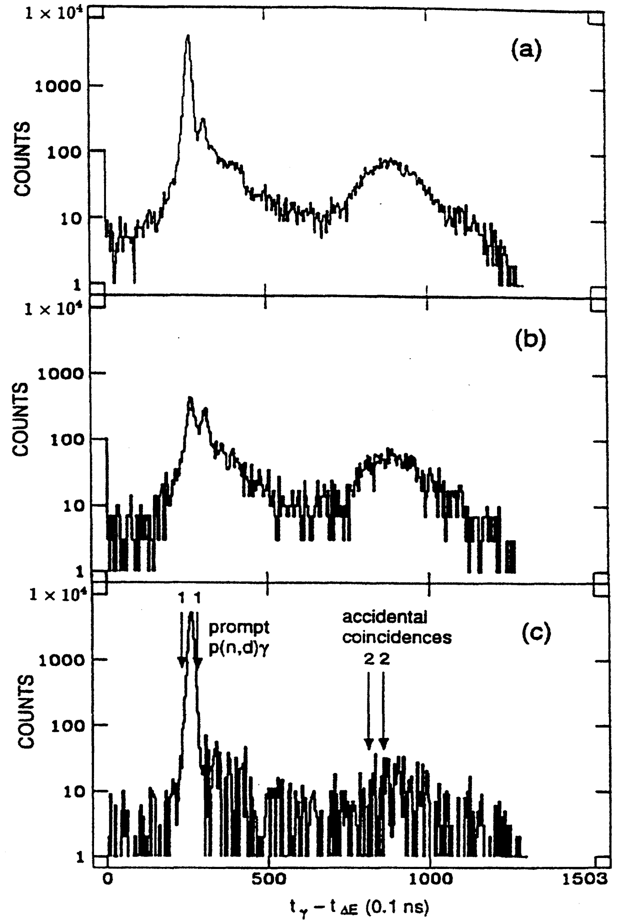

FIG. 3. (a) Time spectrum t_γ-$t_{\Delta E}$ after application of software cuts described in the text for the PPT; (b) same conditions, but for the dummy target, normalized to the same integrated neutron flux as the PPT; (c) the difference of (a) and (b).

The effectiveness and cleanliness of the event selection can be seen from Figs. 3 and 4. Figures 3(a), 3(b) show, on a logarithmic scale, the t_γ-$t_{\Delta E}$ spectra after all software cuts have been applied to other variables (except neutron energy) for the PPT and the dummy target, respectively. The latter spectrum reveals two background peaks of approximately equal size, resulting from quasifree $A(n,d\gamma)$ events on the dummy target and from free $p(n,d)\gamma$ events initiated on the ΔE scintillator. This background ($\sim$10%) was removed by subtracting the (normalized) dummy data from the PPT data, resulting in a very clean, narrow peak that corresponds to the $p(n,d)\gamma$ events induced on the hydrogen component in the PPT, as shown in Fig. 3(c).

Figure 4 shows the ϕ_{open} spectra for the PPT with partial cuts (event origin, particle identification, and timing correlation) and all cuts (except those on neutron energy and coplanarity itself). The former spectrum exhibits a significant accidental coincidence background, whose dependence on ϕ_{open} (roughly sinusoidal) reflects the detector acceptance: Both the d and γ detectors had maximal acceptance for par-

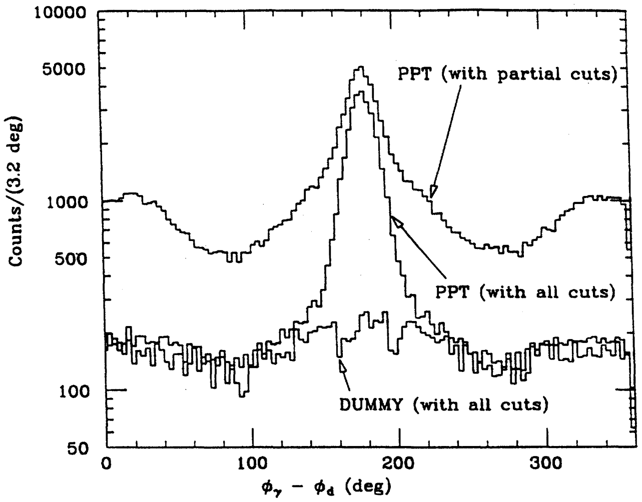

FIG. 4. $\phi_{\text{open}}=\phi_d$-$\phi_\gamma$ spectra for the PPT with partial and all (except the neutron energy and coplanarity itself) cuts, and for the dummy target with all cuts (normalized to the same integrated neutron flux as the PPT).

ticles near the horizontal plane, resulting in an enhanced likehood of d-γ accidentals near ϕ_{open}=0°, 180°, and 360°. Also shown is the corresponding spectrum for the dummy target with all cuts (normalized to the same integrated neutron flux as was used in the PPT bombardment). As is evident from the figure, after applying all cuts and the dummy data subtraction, we are left with a very clean peak centered at 180° in the ϕ_{open} distribution, as expected for a two-body final state. The events observed with the dummy target exhibit only a weak and very broad peak centered at 180°, as appropriate for quasifree $A(n,d\gamma)$ reactions, where the kinematics are smeared by the momentum distribution of the struck protons within target nuclei.

2. Analysis of events with MWPC multiple hits or clear failure

Of the raw $d\gamma$ coincidence events that we acquired, a substantial portion (35% averaged over the entire experiment) involved multiple hits in at least one (in most cases, one or two) of the four wire chambers. The observed fraction of events with multiple hits was correlated with the primary beam current, but was independent of the neutron and proton spin directions. Thus we found that the $np \to d\gamma$ spin observable results extracted with and without inclusion of the multiple-hit events agreed within the statistical uncertainties associated with the questionable events. In order to carry out this comparison and to extract absolute differential cross sections, it was important to understand the nature of the multiple hits and to develop an independently testable algorithm for treating them.

For the vast majority of runs, we observed no significant differences in the scintillator or Čerenkov counter ADC and TDC spectra between the normal events and those with multiple MWPC hits. This observation, together with the rate dependence, suggests that the dominant source of the multiple hits was random coincidences with abundant minimum-ionizing particles produced by the beam. Such particles would not generate their own electronic triggers, but could yield wire chamber hits (with substantially less efficiency than the deuterons) if they occurred within 600 ns after the arrival of a valid event. Their energy depositions in the in-beam scintillators would not have surpassed the thresholds, eliminating corruption of TDC information and adding only a small amount of integrated charge (within the experimental resolution) to the ADC information when they arrived within the 140 ns ADC gate width for a valid event.

A substantial additional source of multiple hit events occurred during four data cycles taken in the second of the three production runs. The extra problem in these cycles was later traced to an intermittent cable connection in the electronic "clear" circuit, which was intended to reset ADC's, TDC's, and wire chamber readout initiated by a scintillator-Čerenkov counter coincidence, when that coincidence was not subsequently accompanied by (slower) signals from three of the four MWPC's. The failing cable resulted in uncleared data being inadvertently recorded in place of the appropriate ADC and TDC information if the next (uncorrelated) event satisfied both the intermediate and the final logic requirements. In the case of the wire chambers, the uncleared hit information was recorded together with the appropriate hits produced by the valid event.

In order to investigate the impact of these problems, in the final production run we purposely removed the MWPC requirement at the trigger logic, thereby eliminating the need for the clear circuit. We instead used a coincidence register bit to record whether at least three MWPC's had fired for each event. The wire chamber hit information was recorded as usual. These data allowed us to simulate in software replay both the ordinary multiple-hit events and the events corrupted by the clear circuit failure, by suitably combining successive events stored on tape. The result of this simulation showed that essentially none of the events with corrupted ADC's and TDC's, caused by the clear circuit failure, could have passed all of the software cuts described in Sec. III B 1. The net effect of the clear circuit failure was thus a reduction in the electronic efficiency for $np \to d\gamma$ events during cycles 18–21, which was shown to be spin independent within statistics. These cycles were excluded from the data sample used for evaluation of absolute differential cross sections.

In the simulation we reproduced the observed properties of the ordinary multiple-hit events well by combining only the MWPC hits for a chain (two or more) of successive events, whenever all but the last in the chain were accompanied by fewer than three MWPC's. Because the ADC and TDC information was uncorrupted, good events could be efficiently recovered by an algorithm that passed any event in which *at least one*, among all possible combinations of MWPC ray tracings, satisfied all of the $np \to d\gamma$ criteria. Application of this algorithm to the artificially corrupted events in the simulation proved highly successful: The valid $np \to d\gamma$ events were recovered with $\leq$0.5% loss and with $\leq$1.5% gain of apparent (but invalid) $np \to d\gamma$ events for each Pb-glass stack and each np spin state. We thus used this multiple-hit event recovery scheme in all of our data analysis, and it provided about 25% of our final $np \to d\gamma$ event sample. The fact that this recovered fraction was the same, within statistics, whether we used loose or tight software cuts to identify the events provides evidence that the

TABLE I. *np* polarimeter results for cycles 14–28, NRM+AFP.

Column	θ_n (deg)	P_n	P_p	P_nP_p	A (this expt.)	A [10,11]
0	33.3	0.5553±0.0034	0.3923±0.0025	0.2179±0.0016	−0.3694±0.0023	−0.384±0.012
1	36.4	0.5582±0.0041	0.3887±0.0029	0.2177±0.0016	−0.2812±0.0021	−0.297±0.009
2	39.5	0.5529±0.0066	0.3988±0.0047	0.2216±0.0021	−0.2020±0.0013	−0.214±0.006
Average	36.2	0.5565±0.0025	0.3921±0.0018	0.2184±0.0010	−0.2902±0.0023	−0.303±0.009

multiple-hit events did not suffer from any significant deterioration of resolution.

C. *np* polarimeter data analysis

1. Identification of np events

The *np* elastic scattering events were identified in software via the following cuts: (a) neutron beam energy, (b) software threshold on the neutron detector pulse height, (c) particle identification (using E^P vs ΔE^P pulse heights to select protons), (d) *np* timing correlation, and (e) accidental coincidence subtraction.

A small fraction ($\simeq$18%) of events accepted by the *np* polarimeter detectors and satisfying the above cuts arose from quasifree $A(n,np)$ reactions on contaminant nuclei in the PPT. This background was subtracted by acquiring *np* polarimeter data using the dummy target, in a way similar to that described in Sec. III B 1.

2. Determination of the beam and target polarizations

Using the extracted *np* polarimeter yields vs *np* spin state, the beam and target analyzing power asymmetries ϵ_n, ϵ_p and spin correlation asymmetry ϵ_{np} for $\vec{n}\vec{p}$ elastic scattering were determined:

$$\epsilon_n \equiv (N_{\uparrow\uparrow}-N_{\downarrow\downarrow}+N_{\uparrow\downarrow}-N_{\downarrow\uparrow})/(N_{\uparrow\uparrow}+N_{\downarrow\downarrow}+N_{\uparrow\downarrow}+N_{\downarrow\uparrow}),$$

$$\epsilon_p \equiv (N_{\uparrow\uparrow}-N_{\downarrow\downarrow}-N_{\uparrow\downarrow}+N_{\downarrow\uparrow})/(N_{\uparrow\uparrow}+N_{\downarrow\downarrow}+N_{\uparrow\downarrow}+N_{\downarrow\uparrow}),$$

$$\epsilon_{np} \equiv (N_{\uparrow\uparrow}+N_{\downarrow\downarrow}-N_{\uparrow\downarrow}-N_{\downarrow\uparrow})/(N_{\uparrow\uparrow}+N_{\downarrow\downarrow}+N_{\uparrow\downarrow}+N_{\downarrow\uparrow}),$$

where the spin-dependent yields N_{ij} are defined as in Sec. I. The beam and target polarizations P_n, P_p could then be deduced from these asymmetries using absolute analyzing power (A_n, A_p) and spin correlation (C_{NN}) values measured for $\vec{n}\vec{p}$ elastic scattering at 183 MeV in a previous experiment [10,11], with absolute normalizations (of uncertainty ±3% for each analyzing power and ±6% for C_{NN}) tied to $\vec{p}\vec{p}$ elastic scattering [10].

The measured ϵ_n and ϵ_p asymmetries have substantial sensitivity to small errors in determining the neutron detector angles (since A_n and A_p vary rapidly as a function of angle within our range [11]) and to instrumental asymmetries in our left-right asymmetric polarimeter (arising, for example, from PPT field effects). In contrast, C_{NN} asymmetries are explicitly left-right symmetric and far less sensitive to field effects, since an average is taken over the two PPT spin directions. Furthermore, for *np* elastic scattering in our angular range, C_{NN} is known [10,11] to vary very weakly with angle: C_{NN}=0.780, 0.732, and 0.690 at the angles $\theta_n^{\mathrm{lab}}=33.3°$, 36.4°, and 39.5°, respectively, of the three neutron detector columns. For the above reasons, we extracted the product P_nP_p, needed to determine C_{NN} for $\vec{n}\vec{p}\rightarrow d\gamma$, directly from the *np* polarimeter spin correlation asymmetry:

$$P_nP_p=\frac{\epsilon_{np}(\theta)}{C_{NN}(\theta)}. \tag{3.1}$$

For individual polarizations, we used the following formulas:

$$A(\theta)=\sqrt{\frac{\epsilon_n(\theta)\epsilon_p(\theta)C_{NN}(\theta)}{\epsilon_{np}(\theta)}}, \tag{3.2}$$

$$P_n=\frac{\epsilon_n(\theta)}{A(\theta)}, \tag{3.3}$$

$$P_p=\frac{\epsilon_p(\theta)}{A(\theta)}. \tag{3.4}$$

In extracting P_n and P_p in this way, we ignore the small (few parts in 10^3) charge-symmetry-violating difference [11] between $A_n(\theta)$ and $A_p(\theta)$ for elastic scattering.

The analysis described above was performed separately for NRM and AFP data and for the three neutron detector columns. Small NRM-AFP differences (~0%, 9%, and 16%, for columns 0, 1, and 2, respectively) were observed in the extracted values of beam polarization P_n and the analyzing power A, but not in P_nP_p, which must reflect the existence of systematic errors associated with the PPT holding field, even after corrections were made in software for the gain shifts observed in the neutron detectors. These errors may arise from the bending of the outgoing proton trajectories in the field, although the proton detectors were made large enough, in principle, to accept the deflected protons for either field orientation. In any case, we assume that the averaging of NRM and AFP results cancels such field-dependent errors to a high degree of accuracy. That this is a good assumption is borne out by the averaged results presented in Table I, where the extracted polarizations are all shown to be independent (within the specified statistical uncertainties) of neutron detector column number, and the extracted analyzing power angular dependence agrees well with earlier measurements [10,11].

For the above reasons, for cycles 1–13 (the first of the production runs), where only NRM data were obtained, we used the *np* polarimeter results extracted from column 0 only, since here the field effect appears negligible; for cycles 14–28, where there were both NRM and AFP data, we used the results extracted from all three columns and averaged over AFP and NRM modes.

D. Evaluation of absolute cross sections for $np \to d\gamma$

The absolute cross sections have been evaluated from the data taken in the final production run only, where the various efficiency and correction factors were best understood. The c.m. frame cross section for np radiative capture ($d\sigma^c/d\Omega$) was deduced from

$$\frac{d\sigma^c}{d\Omega}=\frac{J}{4\Delta\Omega N_H \eta_d \eta_\gamma \eta_s}\sum_{i=1}^{4}\frac{Y_i}{F_i L_{d\gamma i} T_i}, \tag{3.5}$$

where Y_i is the $np \to d\gamma$ yield measured for the ith np spin state and for a given Pb-glass detector stack; J is the Jacobian factor converting the laboratory cross section to the center-of-mass frame; $\Delta\Omega=0.127$ sr is the laboratory solid angle of each Pb-glass stack front face as viewed from the center of the target; $N_H=3.29\times10^{22}\ \mathrm{cm}^{-2}$ is the number of free hydrogen atoms per unit area in the PPT; η_d is the combined efficiency for all the four wire chambers to detect a deuteron ($\eta_d=0.978\pm0.001$ for both the PPT and dummy target runs); η_γ is the photon detection efficiency for a given Pb-glass stack; η_s is the combined efficiency of software cuts used to extract the $np \to d\gamma$ events from the data; F_i is the neutron beam intensity (neutrons/s) for the ith spin state, averaged over all the PPT bombardments; $L_{d\gamma i}\simeq0.92$ is the electronic and computer live time for the $d\gamma$ events obtained with the PPT for the ith spin state; and T_i is the total data acquisition time for the ith spin state for the PPT.

Once $d\sigma^c/d\Omega$ is known, we use the principle of detailed balance to convert this quantity to the c.m. deuteron photodisintegration cross section, $d\sigma^\gamma/d\Omega$, via

$$\frac{d\sigma^\gamma}{d\Omega}=\frac{2}{3}\frac{K_p^2}{K_\gamma^2}\frac{d\sigma^c}{d\Omega}, \tag{3.6}$$

where K_p and K_γ are the proton and photon c.m. momenta, respectively.

The estimation of the factors F_i, η_s, and η_γ involved nontrivial analyses and calibrations, as briefly discussed below.

1. Neutron beam intensity F

The absolute calibration of the neutron beam intensity was based on the known differential cross section [16] and the observed yields of np back-angle elastic scattering events induced in the PPT and in the auxiliary CH_2 target. During the experiment, we acquired events triggered by forward-going protons (prescaled by a factor of 400) simultaneously with the $np \to d\gamma$ events (see Sec. II D). Software cuts on neutron beam energy, event origin, particle identification, and veto (V) detector pulse height and timing were used to identify protons as np backscattering candidates. Most (~80%) of these candidate events arose from quasifree scattering on contaminant nuclei in the PPT (~55%) or from reactions induced on other materials (e.g., the ΔE scintillator) along the beam path (~25%). Thus the dummy target subtraction was critical for determining the true elastic scattering yields associated with the hydrogen in the PPT.

The np backward elastic scattering cross section and its normalization uncertainty [16] is $(d\sigma/d\Omega)_{np}^{\mathrm{lab}}=(31.2\pm3.1)$ μb/sr, averaged over the illuminated solid angle (0.158 sr) of the forward charged particle detectors. Using the above information and the measured lifetimes and wire chamber detection efficiencies, we deduced an average intensity $F=(3.70\pm0.37\pm0.41)\times10^6$ neutrons/s. This was obtained with an average primary proton beam current of 205.7 nA. The two errors quoted for F are both systematic errors and are due, respectively, to the normalization uncertainty in the np scattering cross section and to the uncertainty in the effective dummy target vs PPT thickness ratio ($=1.00\pm0.04$; see Ref. [11]). As a cross-check on the above result, we also took data (subject to less quasifree contamination) with CH_2 and with C targets (see Sec. II), whose thicknesses were more accurately known than those of the PPT and dummy target. Using the same methods as above, from these data we deduced $F=(3.66\pm0.37)\times10^6$ neutrons/s, normalized to the same primary beam current as measured in a Faraday cup, in good agreement with the PPT result. The 10% error in the latter value of F is predominantly due to the np cross section normalization uncertainty. In our experiment we found that the neutron flux (F_i) was proportional to the primary beam current (I_i) monitored by the Faraday cup, and to a good approximation the proportionality constant was independent of the np spin state i. We thus used the values $F_i=(3.66\pm0.37)\times10^6$ [(neutrons/s)$\times(I_i/205.7$ nA)] in the evaluation of $np \to d\gamma$ cross sections.

2. Software cut efficiency η_s

The software efficiency was estimated only for the MWPC "perfect"-hit data, where there was no ambiguity in ray tracing. Although the procedure described below for evaluating η_s is not applicable for the recovered multiple-hit data, we do not expect any significant differences in the distribution of events with respect to kinematic variables, and therefore in η_s, between events with and without accidental extra MWPC hits. This view is supported by the observation that the "perfect"-hit and the multiple-hit samples give the same (within statistics) ratio of yields with tight vs loose software cuts, for each of the eight Pb-glass detector stacks (the ratio averaged over eight stacks is 0.79). In the following analysis, we estimate the efficiency only for the loose cuts which were actually used to extract cross sections.

The efficiencies corresponding to most of the individual software cuts (event origin, particle identification, E_γ, $\Delta\theta$, and E_d vs θ_γ; see Sec. III B) could be determined by taking the difference between two ϕ_{open} distributions (after background and accidental coincidence subtraction). Specifically, we compared the distribution for events satisfying *all* of the software cuts (except for the ϕ_{open} cut itself) to that for events satisfying all *but the one cut* of interest. A narrow peak centered at 180° in this difference spectrum (containing the events removed specifically by the one cut of interest) would indicate that this cut caused a loss of $np \to d\gamma$ events, and the lost yield was then determined from the peak area (over the range $147°\leq\phi_{\mathrm{open}}\leq213°$). This approach could not be used to determine the effects of the ϕ_{open} cut itself or of the t_γ-$t_{\Delta E}$ cut, where it conflicts with the procedure for subtracting accidentals. In these cases, we estimated the losses by fitting the observed peaks with Gaussian distributions and calculating how much of the Gaussian fell outside the corresponding one-dimensional loose gates.

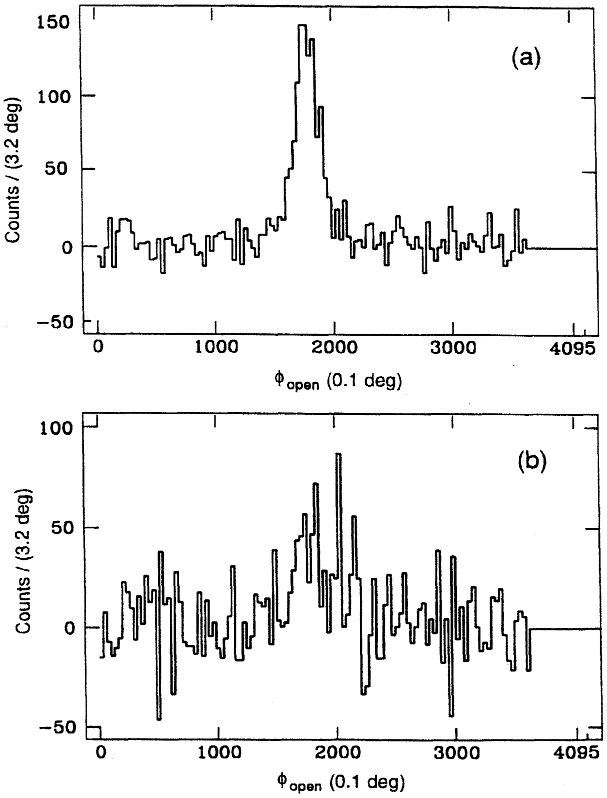

FIG. 5. $np \rightarrow d\gamma$ ϕ_{open} spectra satisfying all but one of the software cuts, and failing: (a) the deuteron particle identification cut; (b) the E_d vs θ_γ cut.

Shown in Fig. 5 are two ϕ_{open} difference spectra containing events removed by a single cut, namely, the particle identification cut in (a) and the E_d vs θ_γ cut in (b). In the former case, the loss peak is obvious, but it is not in the latter. To evaluate the losses quantitatively in each case, we have subtracted one-half of the summed background in the two neighboring regions, $80° \leq \phi_{\mathrm{open}} \leq 147°$ and $213° \leq \phi_{\mathrm{open}} \leq 280°$, from the counts inside the ϕ_{open} peak region defined above. We thus calculated the relative event losses due to each individual cut. We found that the deuteron particle identification cut and the E_d vs θ_γ cut caused the largest losses [$(4.7 \pm 0.3)\%$ and $(2.3 \pm 0.6)\%$, respectively], probably arising in both cases from the reaction tail in the E scintillator. All other cuts combined caused a loss of $(4.2 \pm 1.3)\%$.

It is conceivable that some good events were lost due to correlated effects of more than one cut, so that they would show up only in spectra of events simultaneously failing two or more cuts. We have investigated such correlations in the analysis and have found that the loss of good events which failed simultaneously the deuteron particle identification cut and the E_d vs θ_γ cut was $(1.2 \pm 0.3)\%$, and the losses which simultaneously failed any other combination of cuts were negligible.

By concentrating on events that fail only one cut or only one of the combinations of two or more cuts at a time in the above prescription, we have defined mutually exclusive losses for the various cuts and their combinations; i.e., no single event can show up in more than one of the loss peaks.

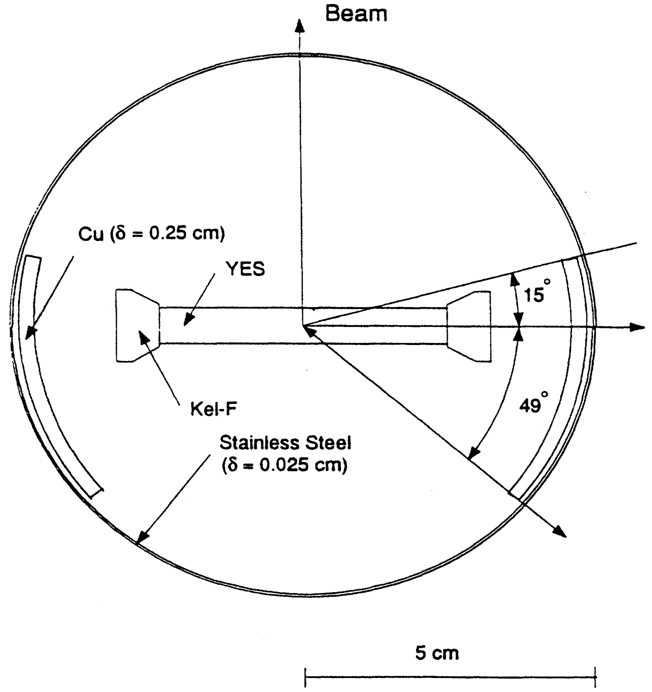

FIG. 6. View from above of the PPT showing the YES target and its Kel-F frame, the stainless steel inner Dewar wall (of thickness $\delta = 0.025$ cm), and the slatted copper plates that were used to aid in the target cooling. The slots in the Cu plates (introduced to minimize eddy current effects) have not been taken into account in the photon attenuation calculations; rather we have simply used an appropriate average thickness ($\delta = 0.25$ cm) of copper. Not shown is an outer aluminum Dewar of radius 14.6 cm and thickness 0.146 cm.

It is thus appropriate to sum the losses as estimated above. The total software cut efficiency for MWPC single-hit data is thus estimated to be $\eta_s = 0.876 \pm 0.014$, where the uncertainty is statistical.

3. Photon detection efficiency η_γ

The photon detection efficiency for a given Pb-glass stack is defined as $\eta_\gamma = N/N_0$, where N_0 is the number of $d\gamma$ photons originally emitted toward the front face of the stack and N is the number actually detected. The efficiency includes the effect of materials inside the PPT Dewar (see Fig. 6), which could convert the photons to e^+e^- pairs before they reached the Pb-glass detectors. For example, using the photon absorption curves in Ref. [17], it was calculated that photons headed for the 86.5° Pb-glass stacks had a probability of $(22 \pm 4)\%$ for such premature conversion. This probability was smaller for the other stacks. The resulting e^+e^- pairs would be bent by the PPT holding field and could be scattered by the materials in the PPT. However, the simulations referred to below indicate that most of the electrons and positrons would still strike the targeted or neighboring Pb-glass counters and would still be recorded as $d\gamma$ photons.

In order to determine the $d\gamma$ photon detection efficiency for the experiment, the GEANT [18] simulation package was used. The simulation used the exact geometry of the Pb-glass

TABLE II. $np \rightarrow d\gamma$ cross sections at $T_n = 183$ MeV and their uncertainties.

θ_γ (lab)	$\theta_{p,\mathrm{c.m.}}$ [a]	Jacobian J	Yield Y	η_γ	$d\sigma^\gamma/d\Omega$ (μb/sr)[b]
116.5	48.9	1.409	2476± 68	0.887±0.040	6.03±0.17±0.29
101.5	62.0	1.232	5730±104	0.890±0.040	6.07±0.11±0.29
86.5	76.0	1.058	6716±108	0.873±0.040	6.24±0.12±0.30
71.5	91.2	0.900	3491± 78	0.902±0.040	5.33±0.12±0.26
56.5	107.7	0.766	3630± 77	0.914±0.040	4.66±0.10±0.22
41.5	125.5	0.662	3328± 74	0.905±0.040	3.72±0.08±0.18

[a] Denoting the angle between the proton momentum and that of the photon in the center-of-mass frame.

[b] The first error in $d\sigma^\gamma/d\Omega$ is statistical; the second is systematic, derived by adding in quadrature the relative uncertainties in those quantities (except the yield Y and the neutron intensity F) shown on the right hand side of Eq. (3.5). We have not included an overall (i.e., angle-independent) normalization uncertainty of ±10%, due primarily to the uncertainty in the absolute np elastic scattering cross section, which was used to determined the absolute neutron intensity F.

arrays (Fig. 1) and a simplified model (Fig. 6) of the materials in the PPT. It incorporated the relevant interaction processes for the photons and their secondary particles in the surrounding materials, and the PPT holding field effect, under the assumption of a uniform magnetic field of 0.059 T with radius of 15 cm centered at the target.

In the simulation, photons were emitted from the target isotropically. Their energies were determined as a function of emission angle from $np \rightarrow d\gamma$ kinematics. For each photon emitted from the target, the simulation tracked the photon and all its secondary particles (i.e., shower) with energies above 0.5 MeV (lower-energy particles contributed negligibly to the total amount of Čerenkov radiation) and recorded energies deposited by these particles in each of the 160 Pb-glass cells. The pulse height in each Pb-glass detector should be approximately proportional to the deposited energy. The pulse height resolution (FWHM) for individual Pb-glass detectors was approximately 45% at $E = 50$ MeV, averaged over the volume of the detector, according to an analysis of the cosmic-ray pulse height spectra taken in the experiment. Since the pulse height resolution is proportional to $E^{-1/2}$, the simulated pulse height was formed by randomizing the deposited energy E (in MeV) according to a Gaussian distribution with a FWHM of $0.45(E/50)^{1/2}$. The requirement for photon detection was the same as in the real experiment, namely, that there be at least one Pb-glass cell whose pulse height exceeds 18 MeV. The cell with the largest pulse height was chosen to determine the photon's angular information.

The calculated photon detection efficiencies η_γ for individual Pb-glass stacks are given in Table II, where the uncertainties are dominated by estimated systematic errors (e.g., errors in the PPT model and in the simulation). The typical efficiency obtained using the GEANT code is 0.89 ±0.04. This is only slightly smaller than the results (0.91) of a very simple calculation using only photon attenuation lengths, in which it was assumed that every photon converted inside the Pb-glass was detected.

According to the simulation, among the events detected by the Pb-glass stacks, a small but sizable portion (≃20% for the 86.5° and 101.5° stacks, and a much smaller portion for the other stacks) were due to the electrons and positrons from conversion inside the PPT, rather than to the direct $d\gamma$ photons. However, according to our calculation and analysis, these electrons and positrons pass the $np \rightarrow d\gamma$ software cuts with almost the same efficiency as the $d\gamma$ photons.

The results of the evaluation of absolute $np \rightarrow d\gamma$ differential cross sections are shown in Table II and Figs. 7, 8, and are discussed in Sec. V.

IV. RESULTS

Shown in Figs. 7, 8 and Table III are our results for the differential cross section $d\sigma/d\Omega$, the neutron and proton analyzing powers A_n and A_p, and the spin correlation coefficient C_{NN} at $T_n = 183$ MeV. The results have been extracted including both the MWPC "perfect"-hit and multiple-hit events, and are based on the loose $\vec{n}\vec{p} \rightarrow d\gamma$ software cuts. For the spin observables, the error bars here represent statistical uncertainties only, but for $d\sigma/d\Omega$ we have added in quadrature all systematic uncertainties other than that governing the overall absolute normalization. The systematic er-

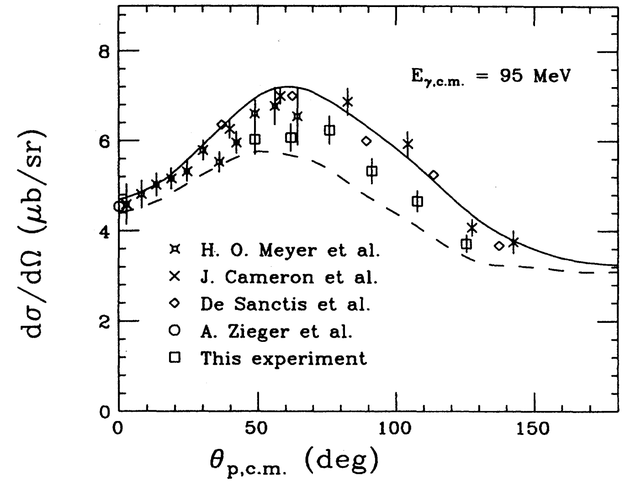

FIG. 7. $d\gamma \rightarrow np$ cross section results of this experiment (in open squares, for which the error bars represent the quadratic sum of all the statistical and systematic uncertainties except the ±10% overall normalization uncertainty). Also shown are previous available data and recent theoretical calculations by Jaus and Woolcock using the Paris N-N potential in impulse approximation with relativistic corrections (dashed curve), plus meson-exchange currents (solid curve).

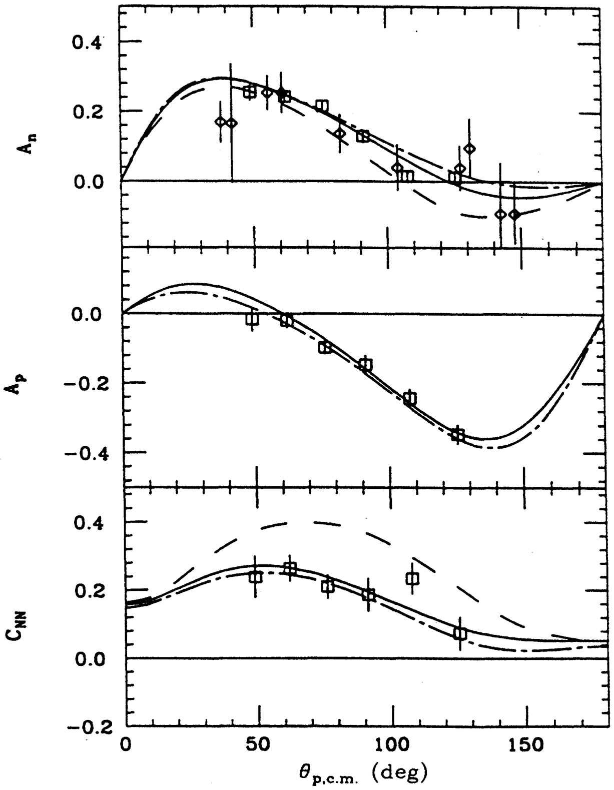

FIG. 8. $\vec{n}\vec{p} \rightarrow d\gamma$ spin observable results of this experiment (open squares). Also shown are previous data for A_n by Cameron *et al.* (open diamonds) and recent theoretical calculations by Jaus and Woolcock (solid and dashed curves, with the same meaning as in Fig. 7) and calculations by Schmitt and Arenhövel (dot-dashed curves) using the Bonn R-space N-N potential, incorporating meson-exchange currents and relativistic corrections.

rors for the spin observables, including the overall normalization uncertainties, are small compared to the statistical uncertainties, and will be discussed in detail in Sec. V.

As can be seen from Table III, the left-right symmetric Pb-glass stacks at $\theta_{\gamma,\mathrm{lab}}=86.5°$ and 101.5° give statistically consistent results for all three spin observables and the cross section, indicating that no significant instrumental asymmetry existed in this experiment. Thus, in Figs. 7, 8 we present results averaged over the left-right symmetric stacks. In deducing the averaged cross sections, we have treated the statistical errors for the left and right stacks as independent, but the systematic errors for the two as completely correlated.

Note that both the theoretical predictions and our measurements (see Fig. 8) for the neutron and proton analyzing powers adhere well to the relation $A_n(\theta_{p,\mathrm{c.m.}})=-A_p(\pi-\theta_{p,\mathrm{c.m.}})$, which should hold in the absence of interfering amplitudes from isospin-0 and isospin-1 np states. While such mixing is forbidden for strong interaction processes by charge symmetry [11], it could arise in principle for the electromagnetic $np \rightarrow d\gamma$ reaction, e.g., from $E1$-$M2$ interference. In practice, however, the most important transitions ($E1$ and $M1$) for this reaction both proceed from isospin-1 (^3P and ^1S, respectively) states, so that the observed relationship between A_n and A_p is not surprising.

For comparison with our data, also shown in Figs. 7, 8 are previous measurements for the cross section [3,19–21] and neutron analyzing power [3]. Our cross section results agree well with all recent measurements at overlapping angles, within our ±10% normalization uncertainty. Our neutron analyzing power results are also in good agreement with the previous data of Cameron *et al.* [3], but exceed their statistical precision by a factor of approximately 3.5.

In Figs. 7, 8 we also show recent predictions by Jaus and Woolcock [6] and by Schmitt and Arenhövel [2]. The dashed curves represent calculations by Jaus and Woolcock using the Paris N-N potential in impulse approximation, along with a relativistic correction to the spin-orbit operator (which is necessary to obtain agreement with the forward angle cross section data). The solid curves, also from Jaus and Woolcock, include additional effects due to explicit coupling between the photon and an exchanged meson (π, ρ, or ω) or an intermediate Δ (1232). These MEC and IC corrections clearly introduce very significant changes in the predicted values of C_{NN} and $d\sigma/d\Omega$, and they must be included to reproduce our measured values. The dot-dashed curves in Fig. 8 represent similar calculations by Schmitt and Arenhövel, but using the Bonn coordinate-space N-N potential. Using four different N-N potentials (Bonn, Paris, Nijmegen, and Argonne V14), Schmitt and Arenhövel have shown [2] that all of the observables reported herein are relatively insensitive to the choice of N-N distorting potential.

The relativistic correction included in all the above calculations has a discernible effect on C_{NN} (as well as on the forward differential cross section) [2] and significantly improves the agreement of the calculations with our measurements.

TABLE III. Results for $\vec{n}\vec{p} \rightarrow d\gamma$ at $T_n=183$ MeV.

$\theta_{\gamma,\mathrm{lab}}$ (deg)	$\theta_{p,\mathrm{c.m.}}$ (deg)	$d\sigma/d\Omega$ (μb/sr)	A_n	A_p	C_{NN}
41.5	125.5	3.72±0.20	0.011±0.020	−0.347±0.028	0.073±0.050
56.5	107.7	4.66±0.24	0.014±0.018	−0.244±0.026	0.234±0.046
71.5	91.2	5.33±0.29	0.129±0.020	−0.147±0.028	0.187±0.050
86.5 (*L*)	76.0	6.02±0.32	0.227±0.020	−0.112±0.029	0.187±0.051
86.5 (*R*)	76.0	6.46±0.34	0.204±0.020	−0.085±0.028	0.230±0.049
101.5 (*L*)	62.0	6.25±0.34	0.225±0.022	0.019±0.032	0.283±0.056
101.5 (*R*)	62.0	5.90±0.32	0.259±0.022	−0.058±0.031	0.246±0.055
116.5	48.9	6.03±0.34	0.255±0.024	−0.017±0.035	0.239±0.061

The new data for $\vec{n}\vec{p} \rightarrow d\gamma$ from this experiment, together with the previous high quality cross section [3,19–21] and photon asymmetry [4,22] data collected over the past decade, place very strong constraints on model calculations. The excellent agreement of the full (i.e., including MEC and IC corrections) Jaus-Woolcock calculation with our results and previous data for all four observables in Figs. 7, 8 is very significant, demonstrating great recent progress in our quantitative understanding of neutron-proton radiative capture at intermediate energies. Similar calculations by Arenhövel *et al.* also reproduce the measurements of the photon asymmetry Σ [4,22] over a range of energies up to the region of the Δ (1232) resonance. The photon asymmetry displays a sensitivity to MEC and IC effects similar to that of C_{NN}, but is more sensitive to the choice of N-N potential, especially to the strength of the tensor force. These quantitative successes at moderate momentum transfer ($q \sim 1$–2 fm^{-1}) make the failures [5] of meson-exchange models of photodisintegration at higher q all the more significant.

V. SYSTEMATIC ERRORS FOR THE $\vec{n}\vec{p} \rightarrow d\gamma$ RESULTS

Sources of systematic error for our $\vec{n}\vec{p} \rightarrow d\gamma$ spin observable results have been studied extensively. Among the many potential sources considered, we found that only three contributed appreciably: (a) the PPT holding field and its reversal, (b) spin-dependent removal of events by software cuts, and (c) uncertainty in the absolute C_{NN} values for np elastic scattering used in the extraction of np polarimeter results. Below we discuss in turn the systematic errors caused by each of these factors.

A. PPT field effects

As was mentioned in Secs. II and III, the PPT holding field caused gain shifts in certain detectors and bending of the deuteron trajectories. We made corrections in the software for both these effects (see Sec. III A). In addition, we acquired data with the PPT in AFP mode, as well as in NRM mode, to partially cancel the remaining field effects.

Upper limits on the level of residual-field-dependent instrumental asymmetries have been estimated in two independent ways. The target analyzing power and spin correlation asymmetries due to instrumental effects were measured directly, by acquiring three cycles of data with the PPT *unpolarized*, but the holding field being reversed as usual (see Sec. II E). The results are close to zero: For example, the absolute value of the $np \rightarrow d\gamma$ target "asymmetry" ϵ_p' (defined as the relative difference in cross sections for the holding field direction up vs down), averaged over the eight Pb-glass stacks for these three cycles is 0.024±0.011. Assuming $|\epsilon_p'| \leq 0.035$, it is calculated that the upper limits of field-dependent systematic errors for A_n, A_p and C_{NN} in a given angle bin (before summing over AFP and NRM data) are less than ±0.005, ±0.083, and ±0.020, respectively. The second method compared polarized target data analyzed separately for NRM and AFP modes, with results shown in Fig. 9. The summed χ^2 value characterizing the agreement between these two sets of spin observable results is 24.1 for a total of 24 data points, suggesting no significant systematic discrepancies. The NRM-AFP differences averaged over the eight Pb-glass stacks for A_n, A_p, and C_{NN} are -0.002 ± 0.015, -0.029 ± 0.022, and 0.010 ± 0.039, respectively.

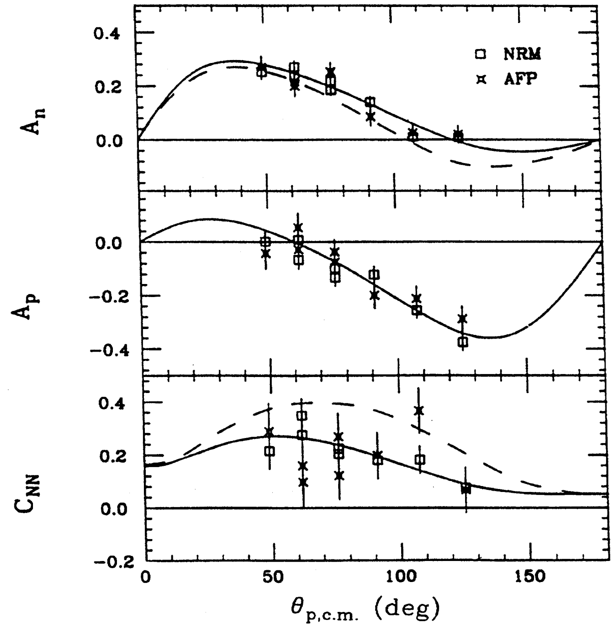

FIG. 9. Comparison of the $\vec{n}\vec{p} \rightarrow d\gamma$ spin observable results extracted separately from NRM and AFP runs. The curves have the same interpretations as those in Fig. 8.

We have used the 1σ statistical fluctuation limits on the results of the above two methods to estimate field-dependent systematic errors in A_n, A_p, and C_{NN}, as determined from the NRM and AFP data alone. In our experiment the ratio between the data acquisition times for AFP and NRM was 3.0/7.0. Because the field effects in these two modes act in opposite directions, summing the AFP and NRM data cancels out the field effects to a large extent, leaving residual errors about 40% as large as those estimated for NRM and AFP alone. After summing NRM and AFP data and combining the results derived via the above two methods, the field-dependent systematic errors for A_n, A_p, and C_{NN} are taken to be ±0.002, ±0.020, and ±0.008, respectively, independent of angle in each case.

B. Spin-dependent removal of events by software cuts

The efficiency of the loose software cuts for selecting $\vec{n}\vec{p} \rightarrow d\gamma$ events was only (87.6±1.4)% (see Sec. III D). Systematic errors will arise if removal of the events by these cuts is spin dependent. In order to estimate the size of such systematic errors, we also extracted $\vec{n}\vec{p} \rightarrow d\gamma$ spin observables with a set of tight software cuts [see Figs. 2(a)–2(h)]. Only the neutron time-of-flight (hence secondary beam energy) gate was left unchanged between the two sets of cuts. We then compared the results corresponding to the tight cuts to the results for the statistically independent events removed upon going from the loose to the tight cuts. The summed χ^2 value obtained by comparing these differences to zero is 26.7 for 24 points.

Detailed comparisons suggest some possible small systematic differences between the loose- and tight-cut results, and these are more likely due to spin-dependent removal of events with the tight software cuts (efficiency $\simeq 71\%$) rather than with the loose cuts. (Although the background is somewhat higher with the loose cuts, the spin observables turn out to be fairly insensitive to background subtraction errors.) We therefore feel the results extracted with the loose cuts are less prone to spin-dependent errors than are the tight-cut results. We take half of the observed rms differences (averaged over the eight Pb-glass stacks) between the tight- and loose-cut results to estimate the systematic errors due to the spin-dependent removal of events by the loose cuts. The associated systematic errors for A_n, A_p, and C_{NN} are ± 0.006, ± 0.013, and ± 0.019, respectively.

C. Normalization uncertainty in *np* elastic scattering C_{NN}

The absolute normalizations for all the polarization results reported here are based on that determined for C_{NN} in $\vec{n}\vec{p}$ elastic scattering in previous experiments [10,11] that utilized the IUCF polarized neutron facility. The C_{NN} calibration in these earlier experiments is subject to an overall normalization uncertainty of $\pm 6\%$ [10], yielding overall normalization uncertainties of $\pm 3\%$, $\pm 3\%$, and $\pm 6\%$, respectively, in A_n, A_p, and C_{NN} measured for $\vec{n}\vec{p} \rightarrow d\gamma$.

D. Summary of systematic errors

Detailed estimates of other systematic errors are given in Ref. [23]. The total systematic errors in the *relative* angular distributions for the $\vec{n}\vec{p} \rightarrow d\gamma$ spin observable results A_n, A_p, and C_{NN}, deduced by adding in quadrature those errors from all sources studied, are no greater than ± 0.007, ± 0.024, and ± 0.022, respectively, in any angle bin. The combined systematic errors are in all cases substantially smaller than the statistical uncertainties. In addition to the systematic errors mentioned above, the $\vec{n}\vec{p} \rightarrow d\gamma$ spin observable results A_n, A_p, and C_{NN} are also subject to overall normalization uncertainties of $\pm 3.2\%$, $\pm 3.3\%$, and $\pm 6.5\%$, respectively. These errors are dominated by the $\vec{n}\vec{p}$ scattering C_{NN} calibration uncertainty described above.

VI. CONCLUSIONS

Measurements of observables for the $\vec{n}\vec{p} \rightarrow d\gamma$ reaction can be used to test our understanding of various important aspects of the strong interaction in the N-N system. In particular, both simple physical arguments and more sophisticated theoretical calculations [2,6] have suggested that, in the intermediate-energy range, the normal-component spin correlation coefficient $C_{NN}(\theta)$ for this reaction is particularly sensitive to electromagnetic currents in which the photon couples *explicitly* to exchanged mesons (MEC's) or to intermediate Δ resonances (IC's). This sensitivity has motivated us to measure $C_{NN}(\theta)$ at $T_n = 183$ MeV, in order to provide a quantitative test for theoretical calculations that incorporate such effects. Our experiment represents the first measurement ever made of two-spin observables in photodisintegration. While measuring C_{NN}, we have also simultaneously measured differential cross sections $d\sigma/d\Omega$, and neutron and proton analyzing powers A_n and A_p.

Our results have been compared with recent theoretical calculations, as well as with previous data for cross sections and neutron analyzing powers. Our cross section results agree well with previous measurements made in the last decade. Our neutron analyzing power results also agree well with the data obtained by Cameron *et al.* [3], but exceed their statistical precision by a factor of 3.5. Most significantly, our results are in excellent agreement with theoretical predictions made (before our experiment) by Jaus and Woolcock, incorporating MEC and IC effects, as well as relativistic corrections [6]. The modifications to C_{NN} that arise from the latter three ingredients are all considerable and are all required in order to obtain the excellent agreement with our measurements. The quantitative agreement found for all measured observables signifies great recent progress in our understanding of MEC, IC, and relativistic effects in the N-N system. Similar theoretical calculations incorporating MEC, IC, and relativistic effects by Schmitt and Arenhövel [2] also agree well with our spin observable data, although they overpredict the cross sections for $\theta_{p,\mathrm{c.m.}} \gtrsim 90°$ by $\sim 20\%$.

In this experiment we have only measured the *normal*-component spin correlation coefficient C_{NN}. Other spin correlation coefficients, such as C_{LL} and C_{SS} (which have not yet been measured), are also expected to be sensitive to MEC and IC effects [2,6]. To provide further constraints on theoretical calculations, it is thus desirable to measure these observables with precision comparable to that obtained in the present experiment. Measurements of tensor polarization observables for deuteron photodisintegration [2] would also be helpful in identifying deficiencies in conventional theory based on nucleon, meson, and isobar degrees of freedom. The failure of such theories, which include only relatively light mesons and only the $\Delta(1232)$ among nucleon resonances, in reproducing the energy dependence of $d(\gamma,p)n$ total cross sections at $E_\gamma > 500$ MeV [5] makes it imperative for future spin experiments (including additional C_{NN} measurements) to explore an energy range above that of the present experiment, where the conventional theory may begin to break down. It will be a challenge to see whether deuteron photodisintegration results over such a broad energy range can eventually be explained within the framework of an extended conventional theory including additional mesons and nucleon resonances in the description, or whether a more efficient treatment can be developed based on quark degrees of freedom.

ACKNOWLEDGMENTS

We would like to acknowledge the contributions of K. Komisarcik and J. Vanderwerp, who operated the liquid deuterium neutron production target and built many of the scintillator detectors. We also acknowledge A. M. Nathan and M. A. Lucas for their assistance in tagged-photon tests of the Pb-glass Čerenkov counters at the University of Illinois. This work was supported in part by the U.S. National Science Foundation under Grants Nos. PHY-9015957, PHY-8611395, and PHY-9103794.

[1] A. J. F. Siegert, Phys. Rev. **52**, 787 (1937).

[2] K.-M. Schmitt and H. Arenhövel, Few-Body Syst. **11**, 33 (1991).

[3] J. M. Cameron *et al.*, Nucl. Phys. **A458**, 637 (1986).

[4] G. S. Blanpied *et al.*, Phys. Rev. Lett. **67**, 1206 (1991).

[5] J. Napolitano *et al.*, Phys. Rev. Lett. **61**, 2530 (1988).

[6] W. Jaus and W. S. Woolcock, Nucl. Phys. **A473**, 685 (1987); **A480**, 573 (1988).

[7] H. Arenhövel and M. Sanzone, Few Body Syst., Supplementum 3, "Photodisintegration of the Deuteron."

[8] M. L. Rustgi, R. Vyas, and O. P. Rustgi, Phys. Rev. C **29**, 785 (1984).

[9] S. F. Pate *et al.*, Phys. Rev. Lett. **70**, 3205 (1993).

[10] T. Bowyer, Ph.D. dissertation, Indiana University, 1994.

[11] S. E. Vigdor, W. W. Jacobs, L. D. Knutson, J. Sowinski, C. Bloch, P. L. Jolivette, S. W. Wissink, R. C. Bird, and C. Whiddon, Phys. Rev. C **46**, 410 (1992).

[12] J. Sowinski and L. D. Knutson, Phys. Rev. B **37**, 9208 (1988); Nucl. Instrum. Methods A **355**, 242 (1995).

[13] W. H. Potter and H. J. Stapleton, Phys. Rev. B **5**, 1729 (1972).

[14] C. Bloch, S. M. Bowyer, T. W. Bowyer, S. F. Pate, and M. A. Pickar, IUCF scientific and technical report, 1990, p. 105.

[15] XSYS Manuals, IUCF version, 1988.

[16] SAID (Scattering Analysis Interactive Dial-in) computer code SAID, R. A. Arndt *et al.*, Fall 1991 version.

[17] TRIUMF Kinematics Handbook, 1987.

[18] GEANT User's Guide, Version 3.15, 1992.

[19] H. O. Meyer, J. R. Hall, M. Hugi, H. J. Karwowski, R. E. Pollock, and P. Schwandt, Phys. Rev. C **31**, 309 (1985).

[20] E. De Sanctis *et al.*, Phys. Rev. Lett. **54**, 1639 (1985).

[21] A. Zieger, A. De Graeve, D. Christmann, R. Van de Vyver, C. Van den Abeele, and B. Ziegler, Phys. Lett. B **287**, 51 (1992).

[22] M. P. De Pascale *et al.*, Phys. Rev. C **32**, 1830 (1985).

[23] G. Xu, Ph.D. dissertation, Indiana University, 1994.